Three-dimensional spectral signal-to-noise ratio for a class of reconstruction algorithms

Pawel A. Penczek[*]

Department of Biochemistry and Molecular Biology, The University of Texas Houston Medical School, 6431 Fannin, MSB6.218, Houston, TX 77030, USA

Abstract

A three-dimensional (3D) version of the spectral signal-to-noise ratio (SSNR)-based resolution measure is introduced. The measure is defined for a class of 3D reconstruction algorithms that use interpolation in Fourier space. The statistical properties of the SSNR are discussed and related to the properties of another resolution measure, the Fourier shell correlation (FSC). The new measure was tested on 3D structures calculated from a simulated set of quasi-evenly spaced 2D projections using a nearest-neighbor interpolation and a gridding algorithm. In the latter case, the results agree very well with the FSC-based estimate, with the exception of very high SSNR values. The main applicability of the 3D SSNR is tomography, where due to the small number of projections collected, FSC cannot be used. The new measure was applied to three sets of tomographic data. It was demonstrated that the measure is sufficiently sensitive to yield theoretically expected results. Therefore, the 3D SSNR opens up the possibility of evaluating the quality of tomographic reconstructions in an objective manner. The 3D distribution of SSNR is of major interest in single-particle analysis. It is shown that the new measure can be used to evaluate the anisotropy of 3D reconstructions. The distribution of SSNR is characterized by three anisotropy indices derived from principal axes of the 3D inertia covariance matrix of the SSNR. These indices are used to construct a 3D Fourier filter which, when applied to a 3D reconstruction of a macromolecule, maximizes the SNR in real space and minimizes real-space artifacts caused by uneven distribution of 2D projections. © 2002 Elsevier Science (USA). All rights reserved.

Keywords: Resolution measures; Electron microscopy; Tomography

1. Introduction

Single-particle analysis has become an established method of structural analysis of large macromolecular complexes. The main advantages are the fact that the molecules can be captured in their native state and, in contrast to X-ray crystallography, the fact that true projections of Coulomb potentials are measured. Therefore, at least in principle, complete information about the mass distribution in the imaged molecule is available. Unfortunately, since the molecules appear randomly oriented on the support grid, it is necessary to establish geometrical relations between various particle views using computational methods. The alignment procedures used are easily affected by the noise in the data. Thus, both the progress made and the reliability of the results must be monitored with the help of so-called "resolution measures" (Frank, 1996), more properly called phase consistency measures.

The available resolution measures fall into two categories: measures based on comparisons of averages calculated for subsets of the data and measures based on averaging of Fourier transforms of individual images. In the first group, we have the differential phase residual (DPR)[1] (Frank et al., 1981) and the Fourier ring correlation (FRC) (Saxton and Baumeister, 1982). A marked advantage of these measures is that they are

---

[1] *Abbreviations used:* 2D, two-dimensional; 3D, three-dimensional; EM, electron microscopy; 3D EM, three-dimensional electron microscopy; DPR, differential phase residual; FRC, Fourier ring correlation; FSC, Fourier shell correlation; SNR, signal-to-noise ratio; SSNR, spectral signal-to-noise ratio.

equally well applicable to two-dimensional (2D) and three-dimensional (3D) data. In the latter case, the volumes resulting from 3D reconstruction algorithms take the place of the 2D averages. What is problematic is that the statistical properties of these measures are not well understood; moreover, they are not applicable in 3D cases where the number of available projections is small, such as tomography. The second group of measures includes the Q-factor (Kessel et al., 1985; van Heel and Hollenberg, 1980) and the spectral signal-to-noise ratio (SSNR) (Unser et al., 1987). Since they operate on Fourier transforms of individual images, statistical properties of the data set are directly captured. The rarely used Q-factor does not yield results that can be expressed as a one-dimensional function of frequency. Recently, the Q-factor was successfully used in the context of refinement of orientation parameters in single-particle analysis (Grigorieff, 1998) and its statistical properties have been subsequently discussed (Grigorieff, 2000). The SSNR for 2D images was introduced by (Unser et al., 1987) and the article contains a detailed analysis of the statistical properties of this measure. The subsequent attempt to extend the measure to 3D was only partly successful, as the approach proposed was based on the estimation of the noise suppression coefficient using a computer simulation approach (Unser et al., 1996).

The lack of a 3D resolution measure that would be applicable to small data sets particularly affects tomography. Since the introduction of the double-tilt tomography (Penczek et al., 1995) and recent efforts to use frozen-hydrated specimens (Baumeister et al., 1999; Baumeister and Steven, 2000; Frey and Mannella, 2000; Mannella et al., 2001; Nicastro et al., 2000), there has been increased interest in this technique. Tomography is particularly valuable because it is applicable not only to isolated particles, but also to larger structures, such as mitochondria, whole cells, and thick sections (up to $10 \, \mu m$) of other biological material. Moreover, unlike in single-particle analysis, the structure can be observed in its unique form, as there is no need for averaging of multiple, individual objects. Thus, the environment of the structure and interactions with membranes and other organelles can be studied. A major limitation of tomography is that the number of 2D projections that can be collected is restricted. Due to radiation dose constraints, the number of projections does not exceed 100–200. Therefore, existing 3D resolution measures (DPR and FSC) are not applicable, as the necessity to split the set of available 2D projections into halves would make the estimate of resolution unreliable.

In what follows, we will demonstrate that a 3D SSNR can be derived for a particular class of 3D reconstruction algorithms. The applicability of the new resolution measure extends beyond tomography, as for single particles it makes it possible to evaluate the resolution anisotropy of 3D reconstructions.

2. Spectral signal-to-noise ratio in two dimensions

2.1. Definition of the 2D SSNR

The spectral signal-to-noise ratio has been introduced in the context of 2D images by (Unser et al., 1987) as

$$\text{SSNR}(R) = \begin{cases} S(R) - 1; & S(R) > 1 \\ 0; & S(R) \leqslant 1, \end{cases} \quad (1)$$

with the spectral variance ratio

$$S(R) = \frac{\sum_{n \in R} \left| \sum_{k=1}^{K} F_k^n \right|^2}{\frac{K}{K-1} \sum_{n \in R} \sum_{k=1}^{K} |F_k^n - F^n|^2}, \quad n = 1, \ldots, n_R, \quad (2)$$

where F_k^n is a 2D Fourier transform of the kth image from a data set of K images, R is the approximately constant spatial frequency region in Fourier space (indexed by n) for which SSNR is evaluated, and

$$F^n = \frac{1}{K} \sum_k F_k^n \quad (3)$$

is the average Fourier component for frequency n. In the same article, it was also shown that for $\text{SSNR}(R) \neq 0$, $S(R)$ has a noncentral F distribution with n_R and $(K-1)n_R$ degrees of freedom and noncentrality parameter $\lambda = n_R \text{SSNR}_T(R)$, where $\text{SSNR}_T(R)$ is the true spectral signal-to-noise ratio of the averaged image. Since the distribution of $S(R)$ can be approximated by a central distribution, it can be shown that its average and variance are well approximated by (Unser et al., 1987)

$$E\{S(R) | \text{SSNR}_T(R)\} \cong \text{SSNR}_T(R) + 1, \quad (4)$$

$$\begin{aligned} \text{Var}&\{S(R) | \text{SSNR}_T(R)\} \\ &\cong 2 \big[(n_R + (K-1)n_R - 2)(1 + 2\text{SSNR}_T(R)) \\ &\quad + n_R \text{SSNR}_T^2(R) \big] / [n_R((K-1)n_R - 4)]. \quad (5) \end{aligned}$$

The 2D SSNR is a one-dimensional function of spatial frequency. In order to use it as a resolution measurement it is enough to choose an arbitrary cut-off level. An appropriate level can be selected as $\text{SSNR}(R) = 1$, the level at which signal and noise powers become equal.

The calculation of 2D SSNR for a set of 2D aligned images is straightforward. The alignment parameters found (relating to translation and rotation) are applied to the original images using an interpolation scheme in real space, 2D Fourier transforms of all images are computed, and the necessary terms in the numerator and denominator of Eq. (2) are calculated. Thus, despite the fact that the interpolation between two grids is required, the images that enter the 2D SSNR calculation are sampled on compatible Cartesian grids.

2.2. Relation between spectral signal-to-noise ratio and fourier ring correlation

FRC, together with its 3D counterpart, Fourier shell correlation (FSC), is the most commonly used resolution measure in single-particle analysis. Therefore, the relation between the FRC and the SSNR is of major interest for practical applications. Is the resolution estimated using either of the measures identical? Is the error (or the variance) of both measures the same? The situation is complicated by the fact that in single-particle analysis, the FSC is used in two different ways. One approach is to derive two "independent" initial reference volumes, split the data set into halves, and then proceed with the 3D refinement of the orientation parameters independently for each set. Another approach is to proceed with the refinement of 3D orientation parameters for all the available 2D projection data simultaneously. In order to monitor the progress, during each refinement cycle the data set is randomly split into halves, and the two volumes are calculated and compared in Fourier space yielding the FSC measure. The obvious questions are the bias implicit in the second approach and whether the first approach is in any way superior.

If the noise in two data sets is independent, which is the case in the first approach to the resolution analysis, it is easy to derive a relation between FRC and SSNR. It is assumed that the signal components in two sets are identical; moreover, the analysis is performed on two averages, F^n and G^n, respectively, each calculated from $L = K/2$ individual images. Thus, we have the definitions

$$F_k^n = F_T^n + N_k^n, \quad G_k^n = F_T^n + M_k^n, \quad n = 1, \ldots, n_R,$$
$$F^n = F_T^n + N^n, \quad G^n = F_T^n + M^n,$$
$$F^n = \frac{1}{L} \sum_{k=1}^{L} F_k^n, \quad G^n = \frac{1}{L} \sum_{k=1}^{L} G_k^n, \quad (6)$$
$$N^n = \frac{1}{L} \sum_{k=1}^{L} N_k^n, \quad M^n = \frac{1}{L} \sum_{k=1}^{L} M_k^n,$$

where we assumed an additive measurement model with F_T^n being the true, unknown signal in the nth Fourier voxel. Assuming Gaussian, independent noise in individual images, we have

$$E[N_k^n] = E[M_k^n] = 0,$$
$$E[N_k^n N_k^{m*}] = E[M_k^n M_k^{m*}] = \delta_{nm} \sigma_N^{n2}, \quad (7)$$
$$E[(N^n)^2] = E[(M^n)^2] = \frac{1}{L} \sigma_N^{n2}.$$

The FRC is defined as

$$\mathrm{FRC}(R) = \frac{\sum_{n \in R} F^n G^{n*}}{\left\{ \left(\sum_{n \in R} |F^n|^2 \right) \left(\sum_{n \in R} |G^n|^2 \right) \right\}^{1/2}},$$
$$n = 1, \ldots, n_R. \quad (8)$$

The extension of FRC to three dimensions is achieved simply by carrying the summation over shells instead of rings, and it is referred to as FSC. With this in mind, the analysis presented below is equally applicable to FSC.

The expectation value of FRC is calculated as

$$E[\mathrm{FRC}] \cong \frac{E\left[\sum_{n=1}^{n_R} F^n G^{n*} \right]}{E\left[\left\{ \left(\sum_{n=1}^{n_R} |F^n|^2 \right) \left(\sum_{n=1}^{n_R} |G^n|^2 \right) \right\}^{1/2} \right]}$$
$$= \frac{\sum_n F_T^{n2}}{\sum_n F_T^{n2} + \sum_n \frac{1}{L} \sigma_N^{n2}} = \frac{\frac{\sum_n F_T^{n2}}{\sum_n \frac{1}{L} \sigma_N^{n2}}}{\frac{\sum_n F_T^{n2}}{\sum_n \frac{1}{L} \sigma_N^{n2}} + 1} = \frac{\mathrm{SSNR}}{\mathrm{SSNR} + 1}. \quad (9)$$

The same relation was derived earlier (Bershad and Rockmore, 1974; Frank and Al-Ali, 1975; Saxton, 1978) in the context of cross-correlation between two real-space images. In addition, in this earlier work the cross-correlation was calculated between individual images, not the averages, as in Eq. (9). Nevertheless, as it follows from Eq. (9), the expectation value of the FRC has the same form in either case. By solving Eq. (9) for SSNR we obtain

$$\mathrm{SSNR} = \frac{\mathrm{FRC}}{1 - \mathrm{FRC}}, \quad (10)$$

which, taking into account that the FRC was calculated from the data set split into halves, must be modified to (Unser et al., 1987)

$$\mathrm{SSNR} = 2 \left(\frac{\mathrm{FRC}}{1 - \mathrm{FRC}} \right). \quad (11)$$

Saxton (1978) also derived the variance of the cross-correlation coefficient, which can be simplified using the relation between the FRC and the SSNR given by Eq. (11):

$$\mathrm{Var}(\mathrm{FRC}) \cong \frac{1}{n_R} \frac{(1 + 3\mathrm{FRC} - 4\mathrm{FRC}^4)(1 - \mathrm{FRC})}{(1 + \mathrm{FRC})^3}. \quad (12)$$

In particular, if there is no signal present (FRC = 0), the variance of the estimate is

$$\mathrm{Var}(\mathrm{FRC}|\mathrm{FRC} = 0) = \frac{1}{n_R}, \quad (13)$$

which is the basis for the often used limit for the resolution tests in single-particle analysis, such as the 3σ test (van Heel, 1987). Nevertheless, if other FRC levels are used as resolution limits, Eq. (12) should be used instead, particularly since the variance of the FRC approaches zero when FRC approaches 1. It is also worth noting that the variance of FRC does not depend on the number of individual images L used to calculate the averages in Eq. (9).

If the FRC is used to estimate SNR level in the data, relation given by Eq. (10) [or (11)] must be used and the

variance of such estimate is (Bershad and Rockmore, 1974):

$$\mathrm{Var}(\mathrm{SSNR}(\mathrm{FRC})) \cong \frac{(1 + 2\mathrm{FRC}/(1 - \mathrm{FRC}))^2}{n_R - 3}$$

$$= \frac{(1 + 2\mathrm{SSNR}(\mathrm{FRC}))^2}{n_R - 3}. \qquad (14)$$

In order to compare it with the variance of the SSNR, we assume that $\mathrm{SSNR} \ll n_R$, which is the case for all but very low frequencies. Under this assumption, Eq. (5) can be simplified to

$$\mathrm{Var}(S) \cong \frac{2}{n_R}(1 + 2\mathrm{SSNR}_T). \qquad (15)$$

In order to directly compare relative errors of SSNR and SSNR (FRC), we plotted two curves, $\sqrt{n_R \mathrm{Var}(\mathrm{SSNR}(\mathrm{FRC}))}/\mathrm{SSNR}$ and $\sqrt{n_R \mathrm{Var}(S)}/\mathrm{SSNR}$, as functions of FRC (Fig. 1). It is remarkable that for very low SSNR in the data (FRC below 0.2), the relative error is smaller for SSNR (FRC) than for SSNR. SSNR yields increasingly more accurate estimates for increasing relative levels of the signal. Moreover, its relative error decreases to zero with increased FRC, while the relative error of SSNR (FRC) decreases to a constant value. Thus, SSNR is a better estimator of the signal-to-noise ratio in the data.

In the second approach to the resolution analysis, the two averages are calculated based on randomly drawn, exclusive samples of the same set of images. In this case, the derivation of Eq. (9) no longer applies, as the relevant estimators must include finite population corrections (Cochran, 1963). As an example, we can calculate expectation values of some of the terms in Eq. (9). If the estimates are based on L elements from the sample of K elements, then

$$E\left[F^n G^{n*}\right] = \frac{K - L}{L}\left(\left|F_T^n\right|^2 - \frac{1}{K}\sigma_N^{n2}\right) \underset{L=K/2}{=} \left|F_T^n\right|^2 - \frac{1}{K}\sigma_N^{n2}, \qquad (16)$$

$$E\left[\left|F^n\right|^2\right] = E^2(F^n) + \mathrm{Var}(F^n)$$

$$= \left|F_T^n\right|^2 - \frac{K - L}{KL}\sigma_N^{n2} \underset{L=K/2}{=} \left|F_T^n\right|^2 - \frac{1}{K}\sigma_N^{n2}. \qquad (17)$$

Based on Eqs. (16) and (17), we can expect that the finite sample correction will introduce a bias into the estimate of FRC and change its variance. Nevertheless, the accuracy of the estimate should increase with the size of the data set K. Indeed, as demonstrated by numerical simulations, the general behavior of the FRC based on the comparison of two random halves of the data set is quite similar to that of the FRC calculated for two independent data sets. In the numerical simulations, in each test a data set containing $n_R \times K$ random, normally distributed numbers was generated with a deterministic signal added such that a predefined signal-to-noise level was achieved. Next, the set was randomly split into halves and the FRC was calculated. The last step was repeated 1000 times using different random halves of the set, yielding the average and the variance of the FRC for the set. The results are included in Table 1. Since the results were only marginally dependent on the number of "images" K (tested for $K = 10, 50, 100, 500, 1000$), only results for
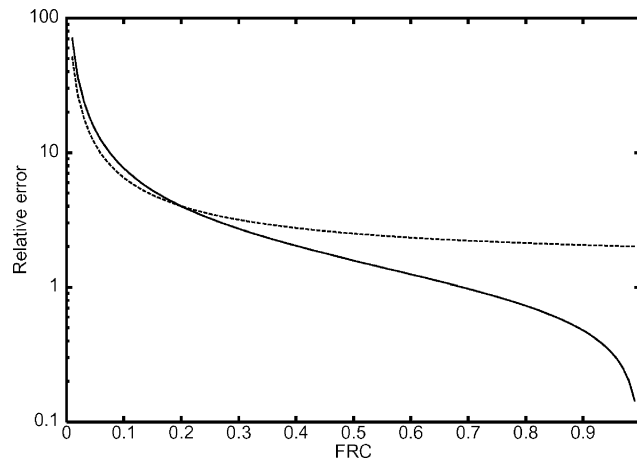
Table 1
Numerical simulations of the variance of the FRC for the FRC estimate based on splitting of the data set into halves

n_R	SNR		
	0.1	1.0	10.0
100	(a) 0.0245	1.32	10.1
	(b) 0.0367	1.34	10.2
	(c) 0.0180	0.401	0.836
	(d) 0.070	0.060	0.021
	(e) 0.097	0.074	0.021
500	(a) 0.0374	0.946	10.3
	(b) 0.0386	0.952	10.4
	(c) 0.0189	0.323	0.838
	(d) 0.033	0.029	0.010
	(e) 0.044	0.033	0.009
1000	(a) 0.0530	0.99	9.99
	(b) 0.0559	0.99	10.0
	(c) 0.0272	0.332	0.833
	(d) 0.022	0.020	0.007
	(e) 0.031	0.023	0.007

Note. The size of the data set used was $n_R \times K$, where $K = 1000$. n_R is the number of samples used to calculate the FRC. SNR is the signal-to-noise ratio set for the simulated data set. (a) Actual SNR of the generated n_R samples. (b) Average SNR in the sample, as estimated by the FRC calculations. (c) Average FRC [(b) is calculated from (c) using Eq. (11)]. (d) Standard deviation of the FRC estimate. (e) Theoretical standard deviation of the FRC according to Eq. (12).

Fig. 1. The relative error (σ_S/S) for two resolution measures. Solid curve SSNR [Eq. (14)]; dashed line FRC [Eq. (12)]. The horizontal axis is plotted in FRC units; the respective SSNR values can be obtained using Eq. (10).

$K = 1000$ are shown. The results demonstrate that the FRC-based estimation of the SNR in the sample, when performed on randomly selected halves of the data set, is quite robust, particularly with an increased number of samples n_R used for the calculation. The value obtained also better approximates the behavior of the true SNR with the increase of the SNR in the data. Very importantly, the standard deviations of the FRC calculated from numerical simulations agree very well with the theoretical standard deviation of FRC, as given by Eq. (12). Again, the agreement improves with increased number of samples n_R and with increased SNR in the data. This demonstrates that the finite sample correction can be ignored in practical 3D EM applications due to the fact that the estimates are calculated from the same data set split into halves.

When the two methods of the resolution estimation are compared, it must be acknowledged that true independence of two subsets of the data set is unlikely to be achieved in practice. The first method, i.e., that based on the separate 3D refinements of the respective halves of the available set of 2D images, is based, like the second method, on the random division of the data set into halves. Nevertheless, unlike in the second method, this division is done prior to the refinement of orientation parameters and subsequent calculation of final 3D structures. Therefore, the refinement procedure becomes an integral part of the resolution estimation. In such a case, at least in principle, the finite sample correction bias is also present, only in this approach the whole refinement procedure should be repeated for various random subsets of the data set if one wants to draw conclusions about its influence on the resolution. Equally unappealing is the realization that when the refinements are performed on data sets reduced by half, the effective SNR in each subset is reduced accordingly; thus, the resulting resolution is unlikely to match the resolution that could be achieved if the refinement was carried out for the whole data set.

3. Spectral signal-to-noise ratio in three dimensions using nearest-neighbor interpolation

Calculation of the SSNR in three dimensions requires consideration of the 3D reconstruction algorithm used to obtain the structure. First, it must be recognized that the data are available in the form of 2D projections of the structure and these projections are—in general— arranged arbitrarily in 3D space. Second, as it follows from the central section theorem, the 2D Fourier transform of a 2D projection of a 3D object forms a central section of the 3D Fourier transform of this object. Thus, it is often more convenient to analyze the problem of 3D reconstruction as a problem of inter-

polation in Fourier space. This interpolation must be performed between 2D Fourier central planes arbitrarily oriented in space and the 3D Fourier Cartesian grid. From this point of view, it becomes clear that the interpolation scheme used or, more generally, the 3D reconstruction algorithm employed, will have a major influence on the quality of the reconstructed object (which in turn can be expressed in terms of 3D SSNR). For most reconstruction algorithms, the noise-reducing effect of the 3D reconstruction procedure must be established empirically. It has been suggested that this can be achieved by calculating a 3D reconstruction using a set of computer-generated noise-only images arranged at the same angles as the available projection data (Unser et al., 1996). The required empirical step remains the major disadvantage of the proposed approach. If, instead, we will restrict our attention to a class of 3D reconstruction algorithms that involve interpolation in Fourier space, the 3D SSNR can be calculated explicitly.

The simplest approach to interpolation is to assign a grid point to the nearest point on the destination grid. Although the quality of this method can be expected to be poor, it remains the fastest approach because there is no need to calculate interpolants. This also significantly facilitates calculation of the 3D SSNR. The only difference in comparison with the 2D case is that due to uneven distribution of 2D planes in 3D space and due to geometrical discrepancies between the two grids, the number of Fourier coefficients per each Fourier voxel will vary. Thus, the average signal in the n'th Fourier voxel is given by

$$F^n = \frac{1}{K_n} \sum_{k=1}^{K_n} F_k^n, \quad n = 1, \ldots, n_R. \tag{18}$$

We assume an additive measurement model

$$F_k^n = F_T^n + N_k^n, \tag{19}$$

where F^n is the unknown signal (independent between frequencies), and N_k^n is a zero-mean noise independent both between frequencies n and measurements k. The expectation value of the power of the signal is

$$E\left[\sum_{n \in R}^{n_R} |F^n|^2\right] = \sum_n \frac{1}{K_n^2} E\left[\left|\sum_k \left(F_T^n + N_k^n\right)\right|^2\right]$$

$$= \sum_n \left\{|F_T^n|^2 + \frac{1}{K_n K_l} \sum_k \sum_l E\left[N_k^n N_l^{n^*}\right]\right\}$$

$$= \sum_n \left(|F_T^n|^2 + \frac{1}{K_n} \sigma_N^{n^2}\right), \tag{20}$$

where $\sigma_N^{n^2}$ is the variance of the noise in the the nth Fourier voxel. The expectation value of the power of the noise $N_k^n = F_k^n - F^n$ is

$$E\left[\sum_n \left|\frac{1}{K_n}\sum_{k=1}^{K_n} N_k^n\right|^2\right]$$

$$= \sum_n \frac{1}{K_n^2} E\left[\sum_k |N_k^n|^2 + \sum_{\substack{k\\k\neq l}} \sum_l N_k^n N_l^{n*}\right] = \sum_n \frac{1}{K_n}\sigma_N^{n2}.$$

(21)

To calculate the expectation value of the ratio of the power of the signal to the power of the noise we neglect higher order terms and approximate it by

$$E\left[\frac{\sum_n |F^n|^2}{\sum_n \left|\frac{1}{K_n}\sum_k^{K_n} N_k^n\right|^2}\right] \cong \frac{E\left[\sum_n |F^n|^2\right]}{E\left[\sum_n \left|\frac{1}{K_n}\sum_k^{K_n} N_k^n\right|^2\right]}$$

$$= \frac{\sum_n \left(|F_T^n|^2 + \frac{1}{K_n}\sigma_N^{n2}\right)}{\sum_n \frac{1}{K_n}\sigma_N^{n2}}$$

$$= \frac{\sum_n |F_T^n|^2}{\sum_n \frac{1}{K_n}\sigma_T^{n2}} + 1 = \text{SSNR} + 1.$$

(22)
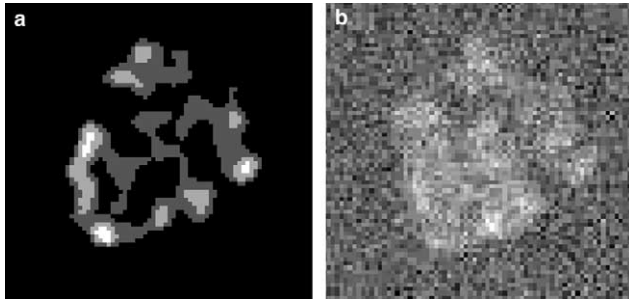
Fig. 2. The central slice of a test 3D structure (modified 70S ribosome from *E. coli*) (a) and one of its projections with Gaussian noise added (b).

Thus, the 3D nearest-neighbor SSNR (SSNR$_{\text{3DNN}}$) is given by

$$\text{SSNR}_{\text{3DNN}} = \frac{\sum_n \left|\frac{1}{K_n}\sum_{k=1}^{K_n} F_k^n\right|^2}{\sum_n \frac{1}{K_n}\sigma_N^{n2}} - 1,$$

(23)

or, using the estimator for the noise variance, by

$$\text{SSNR}_{\text{3DNN}} = \frac{\sum_n \left|\frac{1}{K_n}\sum_{k=1}^{K_n} F_k^n\right|^2}{\sum_n \frac{1}{K_n}\frac{1}{K_n-1}\sum_{k=1}^{K_n} |F_k^n - F^n|^2} - 1.$$

(24)

For simplicity, here and in what follows, we omit the statement SSNR $\geqslant 0$. If we assume the same number of Fourier elements per each voxel, i.e., $K_n = K$, Eq. (24) is reduced to Eqs. (1) and (2); therefore, under this assumption it is equivalent to the 2D case.

In order to test SSNR$_{\text{3DNN}}$, we prepared a nonsymmetric 3D test structure [derived from the previously solved structure of the *Escherichia coli* 70S ribosome (Gabashvili et al., 2000)] modified such that it comprised three different density values (1, 2, and 3). The structure was placed in a cubic volume with a linear size of 75 voxels and the background was set to zero (Fig. 2a). Next, using an angular step of 4° a set of 1253 quasi-evenly spaced 2D projections (Penczek et al., 1994) was calculated and corrupted by independent Gaussian noise resulting in real-space SNR $\cong 5$ (Fig. 2b). Using the known Eulerian angles, this set of 2D projections was used to calculate SSNR$_{\text{3DNN}}$ according to Eq. (24). In addition, the set of 2D projections was randomly split into halves, and two volumes were calculated and compared in Fourier space yielding an FSC-based estimate of the resolution. The results are shown in Fig. 3, where for better comparison two sets of curves are given using either of the relations between SSNR and FSC [Eqs. (10) and (11)]. According to these results, the SSNR$_{\text{3DNN}}$ underestimates resolution in the whole
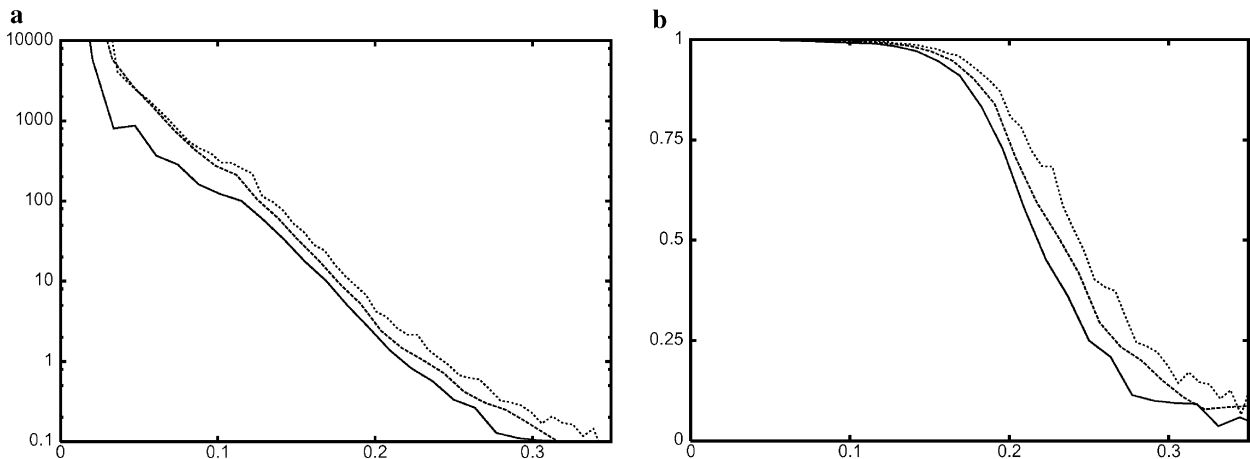

Fig. 3. Test of SSNR$_{\text{3DNN}}$ using simulated test data of 1253 quasi-evenly spaced 2D projections (SNR $\cong 5$). Solid curve, SSNR$_{\text{3DNN}}$; dashed curve, FSC for volumes calculated using the nearest-neighbor interpolation; dotted curve; FSC for volumes calculated using the gridding algorithm. (a) Curves in SSNR units. (b) Curves in FSC units. Horizontal axis is the spatial frequency in absolute units (Nyquist frequency = 0.5).

frequency range. The reason is that $SSNR_{3DNN}$ yields the resolution of the 3D reconstruction as performed using an unsophisticated interpolation scheme in Fourier space. Thus, in addition to the usual resolution-limiting factors, such as the noise in the data and limited number of projections and their particular distribution, the resolution is adversely affected by the additional inaccuracies (noise) caused by the nearest neighbor interpolation.

4. Spectral signal-to-noise ratio in three dimensions using an interpolation scheme

The interpolation in the Fourier domain is a difficult task, as even small interpolation errors in Fourier space tend to produce large artifacts in real space. In principle, a space-limited signal is fully represented by a discrete set of evenly spaced Fourier samples. Consequently, the original Fourier space signal can be recovered at any nonsampled location using a convolution with a sine function (Papoulis, 1962). This, however, is rarely done in practice, as the computational cost is prohibitive. Instead, either a truncated sine function is used or other interpolating kernels are incorporated. In the latter case, a trade-off between the length of the kernel and the size of the interpolation errors is necessary. In the context of EM, a number of such kernels have been proposed: a cubic convolution (Carazo et al., 1986), a moving window Shannon reconstruction incorporating a version of the attenuated sine kernel (Lanzavecchia et al., 1993), and a bilinear interpolation (Grigorieff, 1998). An alternative, but closely related approach to the Fourier domain interpolation is the so-called "gridding algorithm" (O'Sullivan, 1985). In this method, instead of designing a kernel that would minimize real space artifacts, a kernel is chosen such that it has both compact support in the Fourier domain and regular behavior in real-space. Thus, the gridding algorithm comprises three steps: the Fourier grid is convolved with the convolution kernel and the samples on the new, regular grid are recovered; the inverse Fourier transform of the gridded data is calculated; and the interpolation artifacts are corrected by dividing the real-space interpolated function by a Fourier transform of the convolution kernel. A number of possible kernel functions have been proposed (Jackson et al., 1991; Schomberg and Timmer, 1995). It can be demonstrated that even for a very compact convolution kernel (not exceeding a few Fourier pixels) the gridding algorithm, when applied to EM data, results in 3D reconstructions of quality surpassing that of other Fourier interpolation methods (Penczek, in preparation).

When the 3D reconstruction is performed using a Fourier interpolation method, a Fourier voxel on the interpolated, regular 3D grid is obtained as a weighted sum of the Fourier coefficients of the 2D projections, with the weight values depending on the convolution kernel used and geometrical distances between grid points

$$F^n = \frac{\sum_{k=1}^{K_n} W_k^n F_k^n}{W^n}, \tag{25}$$

where $W^n = \sum_{k=1}^{K_n} W_k^n$ is the sum of (positive) convolution weights within the nth voxel. Thus, assuming the additive measurement model [Eq. (19)], the expectation value of the power of the signal for frequency R is

$$E\left[\sum_{n \in R} |F^n|^2\right] = \sum_n E\left[\frac{\left|\sum_k W_k^n F^n + \sum_k W_k^n N_k^n\right|^2}{W^{n^2}}\right]$$

$$= \sum_n \left\{ \frac{W^{n^2}}{W^{n^2}}(F_T^n)^2 + \frac{E\left[\left(\sum_k W_k^n N_k^n\right)^2\right]}{W^{n^2}} \right.$$

$$\left. + 2\frac{\left(\sum_k W_k^n F^n\right)E\left[\sum_k W_k^n N_k^n\right]}{W^{n^2}} \right\}$$

$$= \sum_n \left((F^n)^2 + \frac{\sum_k W_k^{n^2}}{W^{n^2}}\sigma_N^{n^2}\right). \tag{26}$$

Unlike in the nearest neighbor interpolation, the variance term in Eq. (26) contains the ratio of the sum of squared weights to the squared sum of weights. Due to the presence of the weights, the noise component must be estimated using the sum of weighted variances

$$\sum_n \frac{1}{W^n}\sigma_{wN}^{n^2} = \sum_n \frac{1}{W^n}\frac{1}{((K_n-1)/K_n)W^n}\sum_{k=1}^{K_n} W_k^n|F_k^n - F^n|^2, \tag{27}$$

whose expectation value is

$$E\left[\sum_n \frac{1}{W^n}\frac{1}{((K_n-1)/K_n)W^n}\sum_{k=1}^{K_n} W_k^n|F_k^n - F^n|^2\right]$$

$$= \sum_n \frac{1}{W^n}\frac{1}{((K_n-1)/K_n)W^n}E\left[\sum_{k=1}^{K_n} W_k^n F_k^{n^2} - W^n F^{n^2}\right]$$

$$= \sum_n \frac{1}{W^n}\frac{1}{((K_n-1)/K_n)W^n}$$

$$\times \left(W^n F_T^{n^2} + W^n\sigma_N^{n^2} - W^n F_T^{n^2} - \frac{\sum_{k=1}^{K_n} W_k^{n^2}}{W^n}\sigma_N^{n^2}\right)$$

$$= \sum_n \frac{1}{W^n}\frac{1}{((K_n-1)/K_n)}\left(1 - \frac{\sum_{k=1}^{K_n} W_k^{n^2}}{W^{n^2}}\right)\sigma_N^{n^2}. \tag{28}$$

By comparing Eqs. (26) and (28) with Eq. (22), we conclude that in the presence of weights it is impossible to obtain an exact estimate of the 3D SSNR. The reason is the different weighting of the noise variance in Eqs. (26) and (28). Nevertheless, it is possible to calculate the two weight components $\sum_k W_k^{n^2}$ and W^n and redefine the
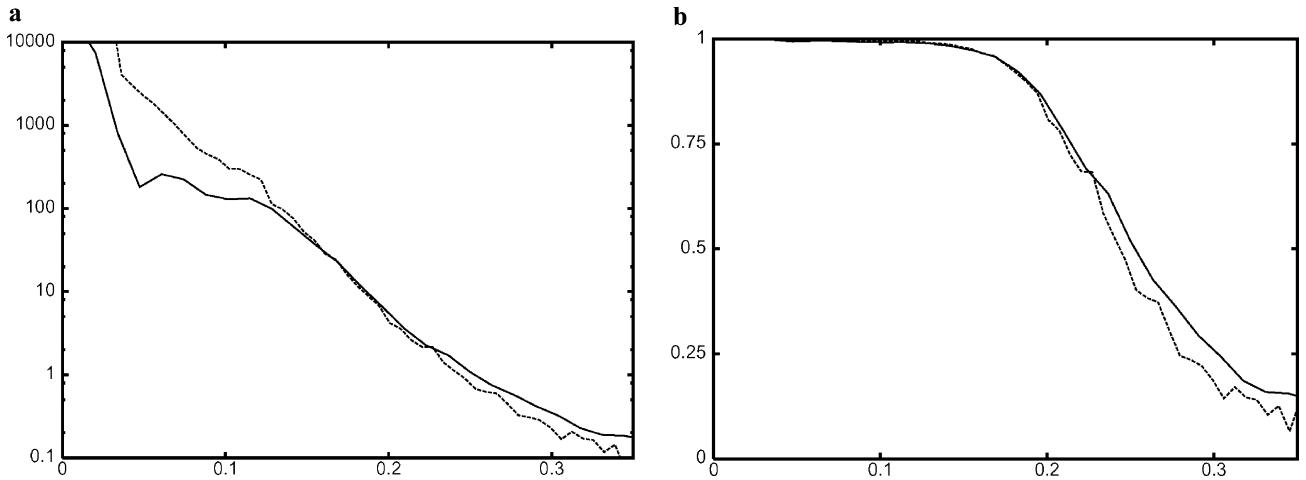
Fig. 4. Test of $SSNR_{3Dw}$ using simulated test data of 1253 quasi-evenly spaced 2D projections (SNR $\cong$ 5). Solid curve, $SSNR_{3Dw}$; dashed curve, FSC for volumes calculated using the gridding algorithm. (a) Curves in SSNR units. (b) Curves in FSC units. Horizontal axis is the spatial frequency in absolute units (Nyquist frequency = 0.5).

"weighted signal" such that the variance components in Eqs. (26) and (28) will have the same expectation value:

$$\frac{E\left[\sum_n \frac{W^n}{\sum_k W_k^{n2}} \left|\frac{\sum_{k=1}^{K_l} W_k^n F_k^n}{W^n}\right|^2\right]}{E\left[\sum_n \frac{1}{W^n} \frac{K_n-1}{K_n} \frac{W^{n2}}{W^{n2}-\sum_{k=1}^{K_n} W_k^{n2}} \sigma_{wN}^{n2}\right]}$$

$$= \frac{\sum_n \frac{W^n}{\sum_k \left(W_k^{n}\right)^2} F_T^{n2} + \sum_n \frac{1}{W^n} \sigma_N^{n2}}{\sum_n \frac{1}{W^n} \sigma_N^{n2}}$$

$$= \frac{\sum_n \frac{W^n}{\sum_k \left(W_k^{n}\right)^2} F_T^{n2}}{\sum_n \frac{1}{W^n} \sigma_N^{n2}} + 1. \qquad (29)$$

If the 3D SSNR were based on Eq. (29), its values would be consistently underestimated by the weight ratio factor that appears in front of the squared "true" signal. Thus, we define the $SSNR_{3Dw}$ for an arbitrary interpolation scheme as

$$SSNR_{3Dw} = \left(\frac{1}{n_R} \sum_{n=1}^{n_R} \frac{\sum_k W_k^{n2}}{W^n}\right)$$

$$\times \left\{\frac{\sum_n^{n_R} \left(\frac{W^n}{\sum_k W_k^{n2}} \left|\frac{\sum_{k=1}^{K_l} W_k^n F_k^n}{W^n}\right|^2\right)}{\sum_n^{n_R} \frac{K_n-1}{K_n} \frac{W^n}{W^{n2}-\sum_{k=1}^{K_n} W_k^{n2}} \sigma_{wN}^{n2}} - 1\right\}. \qquad (30)$$

Equation (30) does not yield "exact" signal-to-noise ratios in the reconstructed volume. This is due to the presence of weights resulting from the convolution with the interpolating kernel. These weights affect signal and noise components differently rendering the exact estimation of the 3D SSNR impossible. Nevertheless, as

demonstrated in the tests performed (see below), the bias present affects mainly very high SSNR values, while in practice, in EM, the low SSNR values are of main interest, as they indicate the resolution limit in a reconstructed structure.

The tests were performed on the same simulated data set used for the testing of $SSNR_{3DNN}$, and the resulting curves are shown in Fig. 4. As indicated above, the $SSNR_{3Dw}$ agrees very well with the FSC-based estimation in the range between SSNR = 0 and SSNR $\cong$ 100. Using Eq. (4), we find that this corresponds to the range of FSC between 0 and 0.99. Thus, in terms of FSC, the bias affects the estimate in the narrow range of very high values that are well above the numbers that are relevant for the analysis of the resolution in 3D EM.

5. Estimation of the resolution of the tomographic reconstructions by the 3D SSNR

The 3D SSNR was applied to the estimation of resolution of three tomographic data sets of plastic-embedded preparations of the Semliki Forest virus in situ (data were kindly provided by Mike Marko and Chyongere Hsieh from Wadsworth Center, Albany, NY) (see Figs. 5 and 6) $SSNR_{3Dw}$ was implemented as defined by Eq. (30) such that the reconstructed volume must be a cube. This does not agree with the reconstruction geometry routinely used in single- and double-axis tomography, where due to the way the specimen is prepared (thin section), the reconstructed volumes are slabs. On the other hand, in many applications of tomography, objects of interests do not fill the reconstructed volume evenly. Instead, we may encounter a number of biologically relevant regions dispersed within a rather featureless environment. Moreover, due to various
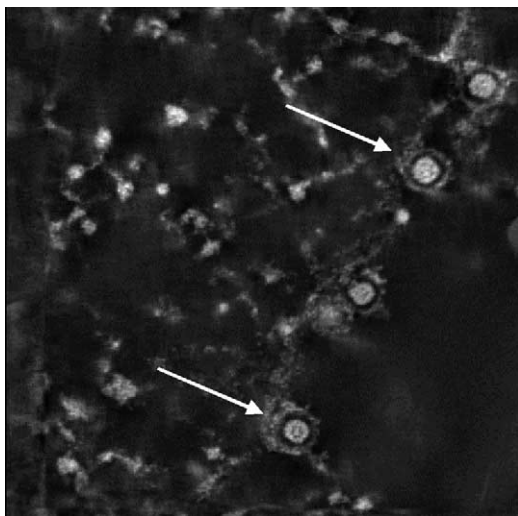
Fig. 5. Selected *z*-slice of a double-tilt reconstruction of Semliki Forest virus. Arrows point to some of the individual virus particles.
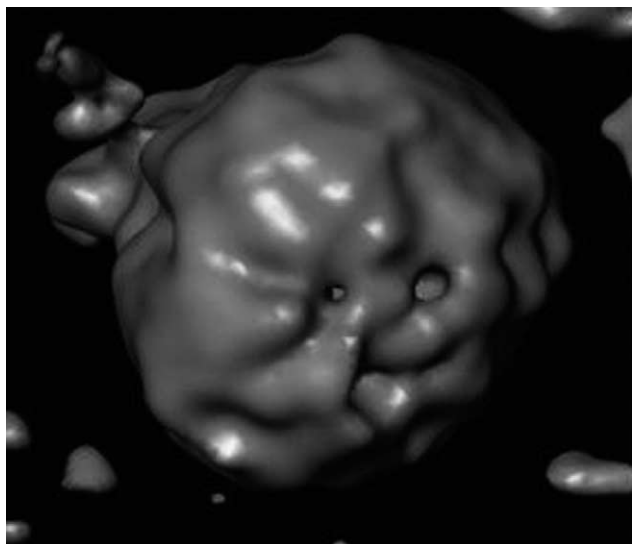

Fig. 6. Double-tilt 3D reconstruction of a selected Semliki Forest virus.

distortions of the specimen during the preparation and microscopy, it can be expected that the resolution is nonuniform within the volume. Therefore, instead of evaluating the resolution for the whole reconstructed volume, it may be preferable to obtain resolution estimates for a number of regions of interest. This approach was chosen in the current implementation of the 3D SSNR. Thus, the estimation of the resolution requires appropriate shifting of 2D projection data so the object of interest is located at the origin of the system of coordinates. Next, the SSNR is estimated within a small cube centered on the object.

The first data set comprised 119 double-tilt images. The *y*-axis series was collected in the range from −60° to +60° and the *x*-axis series in the range from −59° to 56° both in 2° steps. The section thickness was 110 nm. The

accelerating voltage was 400 kV and the pictures were taken in focus. The $SSNR_{3Dw}$ curves were calculated for three selected viruses (Fig. 7a). All three curves are very similar and indicate that there is a pronounced drop in the signal strength beyond 80 Å, although useful information extends to ∼40 Å.

The two remaining data sets were collected in order to test the influence of the section thickness on the resolution. Both were single-axis tilt series; the first was collected in the range from −60° to +60° the second from −60° to +56° both in 1° steps. The section thickness was 110 and 60 nm, respectively, with all other microscopy settings the same as in the case of double-tilt reconstruction. For each set, the 3D SSNR was calculated for two selected viruses (Figs. 7b and c.) The resolution of the 60-nm reconstruction is noticeably better than the resolution of 110 nm and the curve extends to nearly 20 Å. Moreover, the resolution of the double-tilt reconstruction is, as expected, markedly higher than the resolution of the single-tilt reconstruction with the same section thickness. Therefore, it can be concluded that a combination of a better data collection strategy with an appropriate choice of the section thickness should result in further improvement in resolution of the tomographic reconstructions.

6. Evaluation of the resolution anisotropy of single-particle reconstructions by the 3D SSNR

In the single-particle analysis, the structural information about the macromolecule is obtained by averaging multiple copies of various 2D views of presumably the same object. The distribution of orientations of the particle views on the support grid is not determined by the data collection geometry, as in the case of tomography, but by various factors that remain mostly beyond experimental control. These factors may include the hydrophobicity of the macromolecules and their interactions with the supporting grid and with the water surface. As a result, in most cases the distribution of particle views is nonuniform. This has a major impact on the quality of the 3D reconstructions. For some reconstruction algorithms, such a nonuniform distribution of projections may result in directional artifacts, particularly if the reconstruction parameters are not adjusted properly (Boisset et al., 1998). In general, for any reconstruction algorithm, an uneven distribution of projections will result in an uneven distribution of SSNR in the reconstructed volume, which in turn will cause elongation-like artifacts in real space. Therefore, it is essential that the distribution of projections is monitored, particularly during the 3D projection refinement procedure (Penczek et al., 1994). The difficulty is that the relation between the distribution of projections and the associated distribution of SSNR in 3D Fourier space
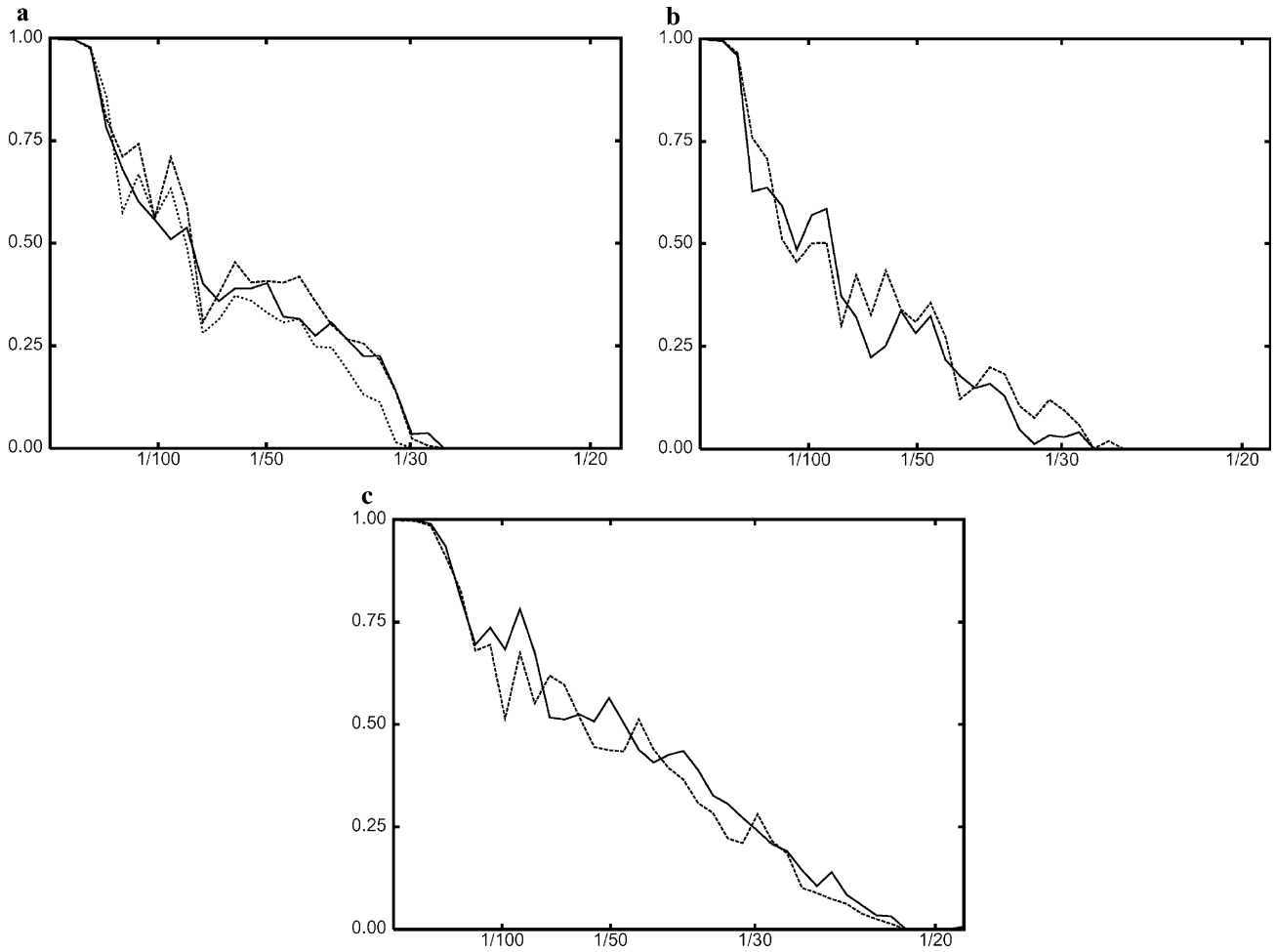
Fig. 7. Resolution estimation for tomographic reconstructions of a Semliki Forest virus in situ. (a) Double-tilt reconstruction, section thickness 110 nm. (b) Single-tilt reconstruction, section thickness 110 nm. (c) Single-tilt reconstruction, section thickness 60 nm.

is not straightforward. For noise-free projection data, it is true that the uniform distribution of projection views is a necessary condition for a full coverage of 3D Fourier space, but the converse is not true. Many possible nonuniform projection geometries result in a full coverage of Fourier space (Orlov, 1976). An extreme example is the full-range single-axis tilt geometry. The situation is even more complicated for projection data corrupted by noise. In such a case, while the distribution of projections is easily evaluated [see Fig. 10 in (Penczek et al., 1994)], the more relevant distribution of signal in 3D Fourier space can be assessed only with the help of the 3D SSNR measure introduced in the previous section.

The SSNR per Fourier voxel is derived as in Eqs. (26)–(30) by omitting the summation over the same-frequency components and is given by

$$\text{SSNR}_w(n) = \frac{\frac{1}{\sum_k W_k^{n^2}} \left| \sum_{k=1}^{K_n} W_k^n F_k^n \right|^2}{\frac{K_n - 1}{K_n} \frac{W^{n^2}}{W^{n^2} - \sum_{k=1}^{K_n} W_k^{n^2}} \sigma_{wN}^{n^2}} - 1. \qquad (31)$$

Equation (31) yields a 3D map of SSNR_w values. The map is centrosymmetric; i.e., $\text{SSNR}_w(\mathbf{k}) = \text{SSNR}_w(-\mathbf{k})$, and thus, its 3D shape can be conveniently characterized by a 3D inertia covariance matrix (Pratt, 1992):

$$\mathbf{C} = \sum_{\mathbf{k}} \text{SSNR}_w(\mathbf{k}) \begin{bmatrix} k_x^2 & k_x k_y & k_x k_z \\ k_x k_y & k_y^2 & k_y k_z \\ k_x k_z & k_y k_z & k_z^2 \end{bmatrix}. \qquad (32)$$

Matrix $\mathbf{C}$ is a symmetric, positive definite matrix; thus, it has three nonnegative real eigenvalues and associated real eigenvectors. The square roots of the eigenvalues $\lambda_1 \geqslant \lambda_2 \geqslant \lambda_3$ correspond to the lengths of principal axes of the ellipsoid that approximates the shape of the distribution of the 3D SSNR, and the eigenvectors yield the directions of the axes. The distribution of the SSNR is characterized by the three anisotropy indices

$$a_u = \frac{\sqrt{\lambda_u}}{\left(\sqrt{\lambda_1} + \sqrt{\lambda_2} + \sqrt{\lambda_3}\right)/3}; \quad u = 1, 2, 3, \qquad (33)$$

with $a_1 = a_2 = a_3 = 1$ meaning the desired, isotropic distribution of the SSNR.

After the 3D reconstruction and corresponding SSNR are calculated, the anisotropy indices and the directions of main axes are used to design a low-pass filter. Unlike standard, spherically shaped filters, a general ellipsoidal shape is used. In this way, the resulting SNR in real space is optimized without inducing undesired artifacts, which might be caused by more complicated filter shapes. For symmetric objects, the SSNR analysis becomes more elaborate, as the segment of the 3D SSNR space corresponding to the unique range of Eulerian angles must be mapped onto whole space. As an example, for the C_n symmetry group the range for the azimuthal angle is $360/n$ degrees. After the inertia covariance matrix is calculated and both the main axes and their directions are found, they must be mapped back into the unique range and the filter is designed as a superposition of multiple ellipsoids.

The distribution of 3D SSNR was calculated and visualized for a set of 3740 Eulerian angles taken from a single-particle analysis of an asymmetric structure (Fig. 8). The anisotropy indices are $a_1 = 1.03, a_2 = 1.01$, $a_3 = 0.97$, where the numbers correspond to the main axes in Fig. 8. Thus, the distribution of the SSNR is slightly flattened and the resolution in the direction of the third main axes is the worst. In terms of real space effects, it can be expected that the structure will be elongated in this direction, while the structural details will be resolved best in the direction of the first main axis
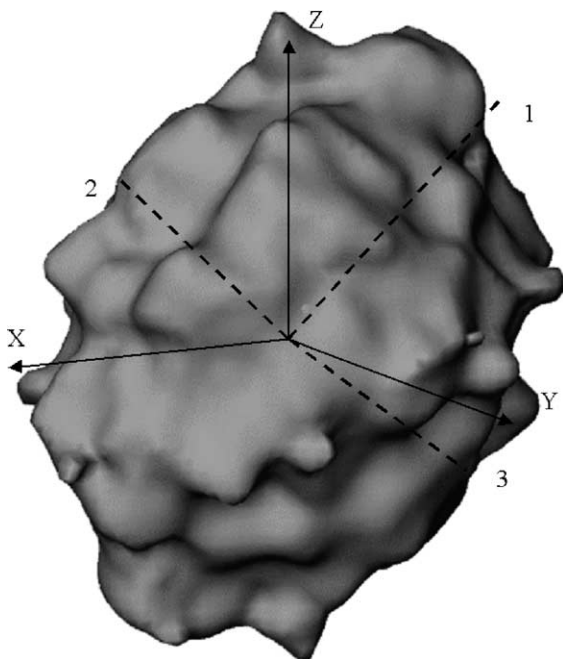

Fig. 8. Three-dimensional distribution of SSNR for a 3D reconstruction calculated using a set of 3740 Eulerian angles taken from a single-particle analysis of an asymmetric structure. *X, Y, Z* indicate the original Cartesian coordinates used to calculate the structure and 3D SSNR. Digits correspond to main axes of the distribution of the 3D SSNR.

of the SSNR distribution. As expected, the directions of the main axes of the SSNR distribution are unrelated to the directions of the original system of coordinates.

7. Conclusions

Measures of consistency of 3D reconstructions are of major importance in single-particle analysis and in tomography. They provide an objective way to evaluate the quality of the results and, when used properly, are helpful in constructing low-pass filters that eliminate excessive noise from the reconstructed structure. Although it is generally agreed that resolution measures are indispensable in single-particle analysis, the practice of resolution estimation varies considerably and it remains a source of intense discussions (van Heel et al., 2000). Briefly, different cut-off levels for resolution claims have been vigorously defended; it remained unclear what was the influence of splitting of the data set into halves for FSC estimation and whether this step should be taken before or after the refinement of orientation parameters; finally, the impact of various image processing steps—including the alignment of the data set itself—has been discussed.

It can be argued that the SSNR provides, at least conceptually, the most straightforward approach to the concept of consistency (or resolution) of the data set. This measure yields ratios of power of the spectral signal to the power of spectral noise for predefined frequency ranges. Thus, in analogy to real-space SNR considerations, the useful information requirement is that the level of signal should exceed the level of noise. This leads to a sensible "resolution" criterion; namely, that the limit of reliable information is at the level of SSNR = 1 or, equivalently, at FSC = 1/3 [see Eq. (11)]. The interpretation of this requirement is unambiguous: due to the linear property of the Fourier transformation, inclusion of Fourier terms with SSNR below 1 will corrupt the real-space map by noise-dominated components.

According to the analysis presented, the SSNR-based estimate of the spectral signal-to-noise ratio in the data set has a lower statistical uncertainty than the FSC-based estimate of this ratio. The exception is the region of very low SNR, in which both measures are largely equivalent. Thus, because there is a direct relation between the two measures, FSC can be used for evaluation of the spectral signal-to-noise ratio in the data set equally as well as the SSNR. Finally, it was demonstrated that the bias in FSC estimation caused by using averages drawn from the same data set is negligible, in terms of both the FSC value and its variance. Thus, it must be concluded that, unless the uncertainty about the performance of the alignment procedure is a factor, the FSC can be applied with high confidence to the resolution estimation of a data set refined as a whole. It also follows that, whenever

applicable, FSC should be given preference over 3D SSNR for the simple reason that FSC can be used for structures obtained with any 3D reconstruction algorithm, while the 3D SSNR was defined only for a class of Fourier space interpolation-based reconstruction methods. The exception is tomography, where due to the small number of projections, FSC would yield misleading results. In this case, 3D SSNR is the only measure that can provide a reliable resolution estimation.

The major shortcoming shared by all the available resolution measures is their inability to distinguish between "true" signal and the correlated noise component (Grigorieff, 2000). The latter is caused by the alignment procedures used to orient in 3D space 2D projections of unknown structure. While the SSNR does not resolve the signal versus noise problem, it yields another important piece of information, namely, the distribution of the variance in 3D Fourier space. This, in principle, should provide a basis for distinction between various contributions to the observed signal.

In addition to resolution as a function of 1D frequency, the 3D SSNR provides an estimate of the signal-to-noise ratio for each Fourier component. Based on the 3D distribution of the SSNR, it is possible to evaluate the anisotropy of the resolution of the 3D structure. As demonstrated, this anisotropy is not necessarily related to the distribution of angular directions of 2D projections used to calculate the structure. Thus, the examination of the distribution of the 3D SSNR is the only possible way to detect related real-space artifacts. The severity of these artifacts can be quantified by the calculation of anisotropy indices of the 3D SSNR map.

The 3D SSNR has been implemented in the SPIDER image processing system (Frank et al., 1996) and the scripts related to the resolution estimation for tomographic reconstructions are available at http://www.wadsworth.org/spider_doc/spider/docs/spider_avail.html.

Acknowledgments

References

Baumeister, W., Grimm, R., Walz, J., 1999. Electron tomography of molecules and cells. Trends Cell Biol 9, 81–85.

Baumeister, W., Steven, A.C., 2000. Macromolecular electron microscopy in the era of structural genomics. Trends Biochem Sci 25, 624–631.

Bershad, N.J., Rockmore, A.J., 1974. On estimating Signal-to-Noise Ratio using the sample correlation coefficient. IEEE Trans. Inf. Theory IT20, 112–113.

Boisset, N., Penczek, P.A., Taveau, J.C., You, V., Dehaas, F., Lamy, J., 1998. Overabundant single-particle electron microscope views induce a three-dimensional reconstruction artifact. Ultramicroscopy 74, 201–207.

Carazo, J.M., Donate, L.E., Herranz, L., Secilla, J.P., Carrascosa, J.L., 1986. Three-dimensional reconstruction of the connector of bacteriophage phi 29 at 1.8 nm resolution. J. Mol. Biol. 192, 853–867.

Cochran, W.G., 1963. Sampling Techniques. Wiley, New York.

Frank, J., 1996. Three-dimensional Electron Microscopy of Macromolecular Assemblies. Academic Press, New York.

Frank, J., Al-Ali, L., 1975. Signal-to-noise ratio of electron micrographs obtained by cross correlation. Nature 256, 376–379.

Frank, J., Radermacher, M., Penczek, P., Zhu, J., Li, Y., Ladjadj, M., Leith, A., 1996. SPIDER and WEB: processing and visualization of images in 3D electron microscopy and related fields. J. Struct. Biol. 116, 190–199.

Frank, J., Verschoor, A., Boublik, M., 1981. Computer averaging of electron micrographs of 40S ribosomal subunits. Science 214, 1353–1355.

Frey, T.G., Mannella, C.A., 2000. The internal structure of mitochondria. Trends Biochem Sci 25, 319–324.

Gabashvili, I.S., Agrawal, R.K., Spahn, C.M., Grassucci, R.A., Svergun, D.I., Frank, J., Penczek, P., 2000. Solution structure of the *E. coli* 70S ribosome at 11.5 Å resolution. Cell 100, 537–549.

Grigorieff, N., 1998. Three-dimensional structure of bovine NADH: ubiquinone oxidoreductase (complex I) at 22 Å in ice. J. Mol. Biol. 277, 1033–1046.

Grigorieff, N., 2000. Resolution measurement in structures derived from single-particles. Acta Crystallographica D Biological Crystallography 56, 1270–1277.

Jackson, J.I., Meyer, C.H., Nishimura, D.G., Macovski, A., 1991. Selection of a convolution function for Fourier inversion using gridding. IEEE Trans. Med. Imaging 10, 473–478.

Kessel, M., Radermacher, M., Frank, J., 1985. The structure of the stalk surface layer of a brine pond microorganism: correlation averaging applied to a double layered lattice structure. J. Microsc. 139, 63–74.

Lanzavecchia, S., Bellon, P.L., Scatturin, V., 1993. SPARK, a kernel software programs for spatial reconstruction in electron microscopy. J. Microsc. 171, 255–266.

Mannella, C.A., Pfeiffer, D.R., Bradshaw, P.C., Moraru, I.I., Slepchenko, B., Loew, L.M., Hsieh, C.-E., Buttle, K., Marko, M., 2001. Topology of the mitochondrial inner membrane: dynamics and bioenergetic implications. IUBMB Life 32, 2–5.

Nicastro, D., Frangakis, A.S., Typke, D., Baumeister, W., 2000. Cryo-electron tomography of neurospora mitochondria. J. Struct. Biol. 129, 48–56.

Orlov, S.S., 1976. Theory of three-dimensional reconstruction. 1. Conditions of a complete set of projections. Soviet Physics-Crystallography 20, 312–314.

O'Sullivan, J.D., 1985. A fast sinc function gridding algorithm for Fourier inversion in computer tomography. IEEE Trans. Med. Imaging MI-4, 200–207.

Papoulis, A., 1962. The Fourier Integral and its Applications. McGraw-Hill, New York.

Penczek, P., Marko, M., Buttle, K., Frank, J., 1995. Double-tilt electron tomography. Ultramicroscopy 60, 393–410.

Penczek, P.A., Grassucci, R.A., Frank, J., 1994. The ribosome at improved resolution: new techniques for merging and orientation

refinement in 3D cryo-electron microscopy of biological particles. Ultramicroscopy 53, 251–270.

Pratt, W.K., 1992. Digital Image Processing. Wiley, New York.

Saxton, W.O., 1978. Computer Techniques for Image Processing of Electron Microscopy. Academic Press, New York.

Saxton, W.O., Baumeister, W., 1982. The correlation averaging of a regularly arranged bacterial envelope protein. J. Microsc. 127, 127–138.

Schomberg, H., Timmer, J., 1995. The gridding method for image reconstruction by Fourier transformation. IEEE Trans. Med. Imaging 14, 596–607.

Unser, M., Trus, B.L., Steven, A.C., 1987. A new resolution criterion based on spectral signal-to-noise ratios. Ultramicroscopy 23, 39–51.

Unser, M., Vrhel, M.J., Conway, J.F., Gross, M., Thevanez, P., Steven, A.C., Trus, B.L., 1996. Resolution assessment of 3D reconstruction by spectral signal-to-noise ratio. In: 11th European Congress on Microscopy, Dublin, Ireland.

van Heel, M., 1987. Similarity measures between images. Ultramicroscopy 21, 95–100.

van Heel, M., Gowen, B., Matadeen, R., Orlova, E.V., Finn, R., Pape, T., Cohen, D., Stark, H., Schmidt, R., Schatz, M., Patwardhan, A., 2000. Single-particle electron cryo-microscopy: towards atomic resolution. Quart. Rev. Biophys. 33, 307–369.

van Heel, M., Hollenberg, J., 1980. The stretching of distorted images of two-dimensional crystals. In: Baumeister, W. (Ed.), Electron Microscopy at Molecular Dimensions. Springer, Berlin, pp. 256–260.